

Realistic triaxial density–potential–force profiles for stellar systems and dark matter halos

Balša Terzić^{1,2} and Benjamin J. Sprague¹

¹*NICADD, Department of Physics, Northern Illinois University, DeKalb, IL 60115, USA*

²*Corresponding Author: bterzic@nicadd.niu.edu*

Received 2007 January 4

ABSTRACT

Popular models for describing the luminosity-density profiles of dynamically hot stellar systems (e.g., Jaffe, Hernquist, Dehnen) were constructed to match the deprojected form of de Vaucouleurs’ $R^{1/4}$ light-profile. However, we now know that elliptical galaxies and bulges display a mass-dependent range of structural profiles. To compensate this, the model in Terzić & Graham was designed to closely match the deprojected form of Sérsic $R^{1/n}$ light-profiles, including deprojected exponential light-profiles and galaxies with partially depleted cores. It is thus applicable for describing bulges in spiral galaxies, dwarf elliptical galaxies, both “power-law” and “core” elliptical galaxies, also dark matter halos formed from Λ CDM cosmological simulations. In this paper, we present a new family of triaxial density-potential-force triplets, which generalizes the spherical model reported in Terzić & Graham to three dimensions. If the (optional) power-law core is present, it is a 5-parameter family, while in the absence of the core it reduces to 3 parameters. The isodensity contours in the new family are stratified on confocal ellipsoids and the potential and forces are expressed in terms of integrals which are easy to evaluate numerically. We provide the community with a suite of numerical routines for orbit integration, which feature: optimized computations of potential and forces for this family; the ability to run simulations on parallel platforms; and modular and easily editable design.

Key words: galaxies: elliptical and lenticular, cD – galaxies: structure – galaxies: nuclei – Galaxy: bulge – galaxies: halos – dark matter

1 INTRODUCTION

Elliptical galaxies, bulges of spiral galaxies and dark matter halos exhibit a range of density-profile shapes which are accurately described by the Sérsic (1963, 1968) $R^{1/n}$ model (e.g. Caon, Capaccioli & D’Onofrio 1993; Young & Currie 1994; Graham et al. 1996; Graham 2001; Balcells et al. 2003; Merritt et al. 2006). This model is a generalization of de Vaucouleurs’ (1948, 1959) $R^{1/4}$ model which provides a decent fit only to galaxies with $M_B \approx -21$ mag (e.g. Kormendy & Djorgovski 1989; Graham & Guzmán 2003). The popularity of de Vaucouleurs’ model permeated into computer modeling of elliptical galaxies: the most popular models used in galaxy dynamics simulations – Jaffe (1983), Hernquist (1990) and Dehnen (1993, see also Tremaine et al. 1994) – were designed to approximate the $R^{1/4}$ light profile when projected. All three of these density models are double power-law models and have the same fixed outer profile slope, declining with radius as r^{-4} . This means that, while undeniably useful, these models are limited in their ability to model realistic

galactic structures and their evolution (Terzić & Graham 2005).

More sophisticated power-law models have since been developed to allow for more flexibility in matching deprojected galaxy light profiles. A 3-parameter Dehnen double power-law model was generalized by Zhao (1996) into a 5-parameter model such that both the inner and outer power-law slope can be adjusted, along with the radius, density and sharpness of the transition region. This model was first introduced by Hernquist (1990, his equation 43) and has the same structural form as the “Nuker” model (e.g., Lauer et al. 1995). However, Graham et al. (2003) show that such double power-law models do not provide an adequate description of profiles with logarithmic curvature, i.e. profiles without inner and outer power-laws which is the case for the luminosity-density profiles of most elliptical galaxies and bulges. The 3-parameter model of Prugniel & Simien (1997) was, however, designed to describe profiles with curvature and does therefore not suffer from such a problem. Their density model provides a good analytic approximation to the deprojected Sérsic $R^{1/n}$ model.

These expressions have proven useful for describing the density profiles of dark matter halos simulated in cosmological models of hierarchical structure formation (Merritt et al. 2006; Graham et al. 2006). Merritt used techniques from nonparametric function estimation theory to extract the density profiles, and their derivatives, from a set of N -body halos, to show that the 3-parameter Prugniel–Simien density profile provides a better description to the data than other 3-parameter models currently in use, such as the generalized NFW (Navarro, Frenk, & White 1996) model with arbitrary inner slope.

Recently, Terzić & Graham (2005) developed a 5-parameter model which is able to unite properly the domain of the black hole with the outer parts of the galaxy. It modifies the 3-parameter Prugniel–Simien density model to allow for (optional) partially depleted power-law cores, providing excellent match to the deprojected light profiles of elliptical galaxies, including the ones with depleted cores for which the Prugniel–Simien model is inadequate. Expressions for the potential and forces corresponding to the spherical Prugniel–Simien model are reported in Terzić & Graham (2005).

Double power-law models owe a good deal of their popularity to the fact that the expressions for the potential and forces are relatively simple, in some cases even expressible in terms of analytic functions. This leads to easy implementation of computer routines for orbital integration. In the trade-off between faithfulness to the physical problem (as measured by how accurately these density profiles match the observed deprojected light-profiles of elliptical galaxies) on one side, and numerical simplicity and computational efficiency on the other, these models favor the latter. However, after more than two decades of rapid progress in computer technology since the first of these models was devised, this choice becomes more difficult to justify. Here we propose to bias the trade-off in the opposite direction – we devise a more realistic physical model at the cost of making it mathematically more intricate and computationally more demanding. Our rationale is that if we are to construct realistic models of galaxies, it is imperative that we use a model capable of reflecting, as accurately as possible, what is observed in Nature. We then estimate computational efficiency of this realistic model and compare it to that of traditional power-law models. Finally, we design and make freely available an optimized suite of computer programs used for orbit integration, in hope to eliminate numerical implementation as an adverse factor.

In this paper we generalize spherical profiles of Terzić & Graham (2005) to three dimensions by replacing radial with ellipsoidal symmetry in the mass density. The outline of the new triaxial model in the context of our earlier work is shown in Fig. 1. In Section 2, the new triaxial model is presented: we start with ellipsoidally stratified mass density distribution and derive the corresponding potential and forces, including special cases when the 5-parameter model reduces to a 3-parameter deprojected Sérsic profile with no power-law core in Section 2.3 and 2-parameter power-law in Section 2.4. The potential and forces are derived in terms of integrals, which are easy to evaluate numerically. In Section 3, we outline the main features of the numerical suite used for orbital integration in the new potential, including code optimization and parallelization, user interface and in-

formation analysis. In Section 4, we use the new model to describe the bulge at the center of the Milky Way as well as a pair of galaxy profiles. We also compare its speed and the goodness of fit to the popular Dehnen model (Dehnen 1993; Tremaine et al. 1994). Finally, we summarize and discuss the importance of the model presented here in Section 5.

2 TRIAXIAL MODEL

In this Section we introduce a family of expressions associated with the spatial density profiles of triaxial stellar systems having Sérsic-like profiles with optional power-law cores, generalizing our earlier work on equivalent spherically symmetric profiles (Terzić & Graham 2005). We derive *exact* expressions for the potential and forces associated with this family of spatial density profiles in terms of quadratures. This profile subsumes two other profiles as its special cases: the 3-parameter Prugniel–Simien profile in the limit of the break radius $r_b \rightarrow 0$, and the 2-parameter power-law core in the limit of $r_b \rightarrow \infty$.

2.1 Density

The triaxial mass density model is a triaxial generalization to the spherical model of Terzić & Graham (2005) model. Replacing radial dependence with a dependence on an ellipsoidal coordinate m , defined as

$$m \equiv \sqrt{\frac{x^2}{a^2} + \frac{y^2}{b^2} + \frac{z^2}{c^2}}, \quad (1)$$

yields a profile with equidensity surfaces stratified on confocal ellipsoids with axis ratios $a : b : c$

$$\rho(m) = \begin{cases} \rho_b \left(\frac{r_b}{m}\right)^\gamma & \text{if } m \leq r_b \\ \rho_b \bar{\rho} \left(\frac{m}{R_e}\right)^{-p} e^{-b_n(m/R_e)^{1/n}} & \text{if } m > r_b \end{cases} \quad (2)$$

with

$$\bar{\rho} = \left(\frac{r_b}{R_e}\right)^p e^{b_n(r_b/R_e)^{1/n}}. \quad (3)$$

Parameters above are defined in the context of the spherical model and its fits to the observed light profiles (Terzić & Graham 2005). The break radius r_b marks the position of instantaneous transition from one regime to another. ρ_b is the density at the break radius. γ is the inner power-law slope, not to be confused with incomplete gamma function $\gamma[a, x]$ defined later in the text. R_e is the (projected) effective half-light radius when $r_b = 0$. The parameter n is the Sérsic index and describes the curvature of the profile. The term b_n is not a parameter, but instead a function of n and chosen to ensure R_e contains half the (projected) galaxy light. It is obtained by solving the equation $\Gamma[2n] = 2 \gamma[2n, b_n]$, where

$$\Gamma[a] = \int_0^\infty e^{-t} t^{a-1} dt, \quad (4)$$

$$\gamma[a, x] = \int_0^x e^{-t} t^{a-1} dt, \quad a > 0 \quad (5)$$

$$\Gamma[a, x] = \Gamma[a] - \gamma[a, x] = \int_x^\infty e^{-t} t^{a-1} dt, \quad a > 0 \quad (6)$$

are the complete, incomplete and complement to the incomplete gamma functions, respectively. A good approxi-

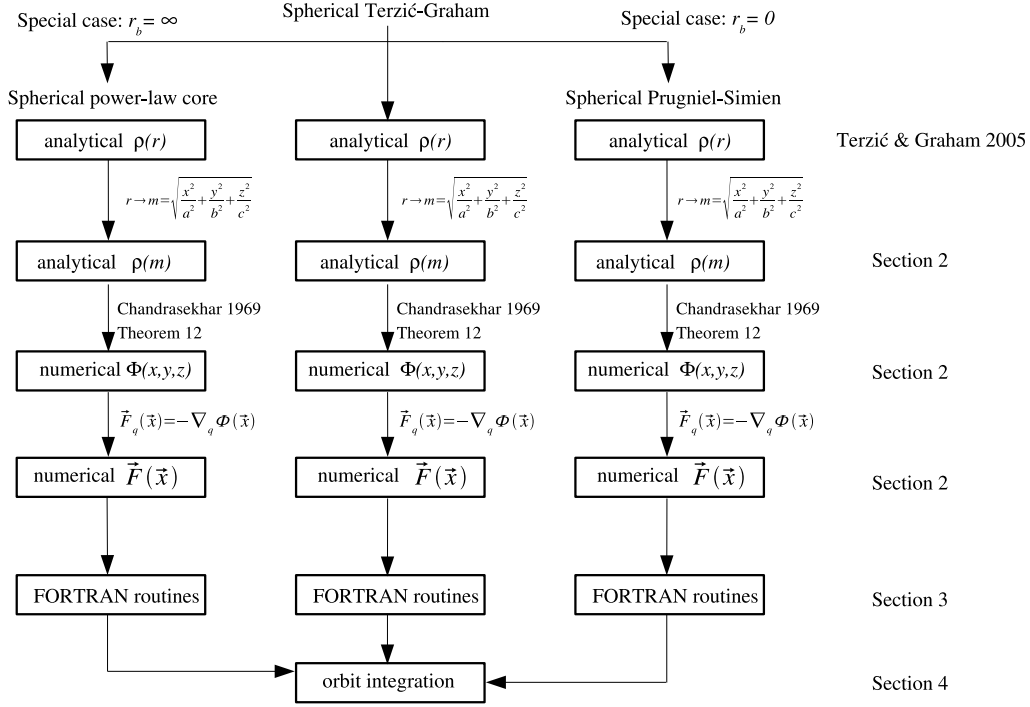


Figure 1. Flow-chart outlining the work presented here.

mation of b_n for $n > 0.5$ is $2n - 1/3 + 0.009876/n$ (Prugniel & Simien 1997; see MacArthur, Courteau, & Holtzman 2003 for smaller values of n). Similarly to b_n , p is also not a parameter, but a function of n , well approximated by $p = 1.0 - 0.6097/n + 0.05563/n^2$, for $0.6 < n < 10$.

2.2 Potential and Forces

The potential arising from an ellipsoidally stratified density distribution $\rho = \rho(m^2)$ can be written as (Chandrasekhar 1969, page 52, Theorem 12):

$$\Phi(x, y, z) = -\pi abcG \int_0^\infty \frac{\psi(\infty) - \psi(\bar{m}^2)}{\sqrt{(\tau + a^2)(\tau + b^2)(\tau + c^2)}} d\tau, \quad (7)$$

with

$$\bar{m}^2(\tau) = \frac{x^2}{a^2 + \tau} + \frac{y^2}{b^2 + \tau} + \frac{z^2}{c^2 + \tau}, \quad (8)$$

and

$$\psi(m^2) = \int_1^{m^2} \rho(\tilde{m}^2) d\tilde{m}^2. \quad (9)$$

After some algebra, we find for $\gamma \neq 2$:

$$\begin{aligned} \Phi(x, y, z) &= \frac{\alpha}{2 - \gamma} r_b^\gamma H(x, y, z; a^2, b^2, c^2, 2 - \gamma) \\ &+ \alpha K R(x, y, z; a^2, b^2, c^2), \end{aligned} \quad (10)$$

when $m \leq r_b$, and

$$\begin{aligned} \Phi(x, y, z) &= \frac{\alpha}{2 - \gamma} r_b^\gamma H^I(x, y, z; a^2, b^2, c^2, 2 - \gamma, \tau_b) \\ &+ \alpha K R^I(x, y, z; a^2, b^2, c^2, \tau_b) \\ &- \alpha n \bar{\rho} R_e^2 b_n^{n(p-2)} T(x, y, z; a^2, b^2, c^2, \tau_b), \end{aligned} \quad (11)$$

when $m > r_b$, where

$$\alpha = 2\pi abcG\rho_b \quad (12)$$

$$K = -\frac{1}{2 - \gamma} r_b^2 - n \bar{\rho} R_e^2 b_n^{n(p-2)} \Gamma \left[n(2 - p), b_n \left(\frac{r_b}{R_e} \right)^{1/n} \right], \quad (13)$$

$$H^I(x, y, z; A, B, C, q, s) \equiv \int_s^\infty \frac{\bar{m}^q d\tau}{d_1(\tau; A, B, C)}, \quad (14)$$

$$H(x, y, z; A, B, C, q) \equiv H^I(x, y, z; A, B, C, q, 0), \quad (15)$$

$$R^I(A, B, C, s) \equiv \int_s^\infty \frac{d\tau}{d_1(\tau; A, B, C)}, \quad (16)$$

$$R(A, B, C) \equiv R^I(A, B, C, 0), \quad (17)$$

$$T(x, y, z; A, B, C, s) \equiv \int_0^s \frac{\Gamma \left[n(2 - p), b_n \left(\frac{\bar{m}}{R_e} \right)^{1/n} \right] d\tau}{d_1(\tau; A, B, C)}, \quad (18)$$

and

$$d_1(\tau; A, B, C) \equiv \sqrt{(\tau + A)(\tau + B)(\tau + C)}. \quad (19)$$

Superscript I denotes an improper integral with a finite non-zero lower limit and infinity as an upper limit. $R(A, B, C)$ is known as Carlson integral (Carlson 1988). τ_b is found by solving a cubic equation $r_b = \bar{m}(\tau_b)$.

For $\gamma = 2$, the expressions for potential are:

$$\begin{aligned} \Phi(x, y, z) &= \alpha r_b^2 H_1(x, y, z; a^2, b^2, c^2) \\ &+ \alpha K_2 R(a^2, b^2, c^2), \end{aligned} \quad (20)$$

when $m \leq r_b$, and

$$\begin{aligned} \Phi(x, y, z) &= \alpha r_b^2 H_1^I(x, y, z; a^2, b^2, c^2, \tau_b) \\ &+ \alpha K_2 R^I(a^2, b^2, c^2, \tau_b) \\ &- \alpha n \bar{\rho} R_e^2 b_n^{n(p-2)} T(x, y, z; a^2, b^2, c^2, \tau_b), \end{aligned} \quad (21)$$

when $m > r_b$, where

$$K_2 = -r_b^2 \log r_b - n \bar{\rho} R_e^2 b_n^{n(p-2)} \Gamma \left[n(2-p), b_n \left(\frac{r_b}{R_e} \right)^{1/n} \right], \quad (22)$$

and

$$H_1^I(x, y, z; A, B, C, s) \equiv \int_s^\infty \frac{\log \bar{m} d\tau}{d_1(\tau; A, B, C)}, \quad (23)$$

$$H_1(x, y, z; A, B, C) \equiv H_1^I(x, y, z; A, B, C, 0). \quad (24)$$

The gravitational forces for $\gamma \neq 2$ are given by

$$F_{q_i}(x, y, z) = -\alpha r_b^\gamma q_i H_2(x, y, z; k_i^2, a^2, b^2, c^2, -\gamma), \quad (25)$$

when $m \leq r_b$ and

$$\begin{aligned} F_{q_i}(x, y, z) &= -\alpha r_b^\gamma q_i H_2^I(x, y, z; k_i^2, a^2, b^2, c^2, -\gamma, \tau_b) \\ &- \alpha \bar{\rho} q_i S(x, y, z; k_i^2, a^2, b^2, c^2, \tau_b), \end{aligned} \quad (26)$$

when $m > r_b$. $k_1 = a$, $k_2 = b$, $k_3 = c$ and $q_1 = x$, $q_2 = y$, $q_3 = z$. The quadratures in the above expressions are defined as

$$H_2^I(x, y, z; D, A, B, C, q, s) \equiv \int_s^\infty \frac{\bar{m}^q d\tau}{d_2(\tau; D, A, B, C)}, \quad (27)$$

$$H_2(x, y, z; D, A, B, C, q) \equiv H_2^I(x, y, z; D, A, B, C, q, 0), \quad (28)$$

$$S(x, y, z; D, A, B, C, s) \equiv \int_0^s \frac{\left(\frac{\bar{m}}{R_e}\right)^{-p} e^{-b_n \left(\frac{\bar{m}}{R_e}\right)^{1/n}} d\tau}{d_2(\tau; D, A, B, C)}, \quad (29)$$

where

$$d_2(\tau; D, A, B, C) \equiv (\tau + D) d_1(\tau; A, B, C). \quad (30)$$

For $\gamma = 2$, no special care in derivation of forces is needed, so they coincide with equations (25) and (26).

The expressions (14), (16), (23), (27) and (18), as well as (29) when $s \rightarrow \infty$, are improper integrals and are not very suitable for numerical computation. This problem is resolved by introducing a new variable of integration $\xi = (1 + \tau)^{-1/2}$. The integrals then become proper and are given by

$$H^I(x, y, z; A, B, C, q, s) = 2 \int_0^{\frac{1}{\sqrt{1+s}}} \frac{\bar{m}^q d\xi}{\tilde{d}_1(\xi; A, B, C)}, \quad (31)$$

$$R^I(A, B, C, s) = 2 \int_0^{\frac{1}{\sqrt{1+s}}} \frac{d\xi}{\tilde{d}_1(\xi; A, B, C)}, \quad (32)$$

$$T(x, y, z; A, B, C, s) = 2 \int_0^{\frac{1}{\sqrt{1+s}}} \frac{\Gamma \left[n(2-p), b_n \left(\frac{\bar{m}}{R_e} \right)^{1/n} \right] d\xi}{\tilde{d}_1(\xi; A, B, C)}, \quad (33)$$

$$H_1^I(x, y, z; A, B, C, s) = 2 \int_0^{\frac{1}{\sqrt{1+s}}} \frac{\log \bar{m}^q d\xi}{\tilde{d}_1(\xi; A, B, C)}, \quad (34)$$

$$H_2^I(x, y, z; D, A, B, C, q, s) = 2 \int_0^{\frac{1}{\sqrt{1+s}}} \frac{\bar{m}^q \xi^2 d\xi}{\tilde{d}_2(\xi; D, A, B, C)}, \quad (35)$$

$$S(x, y, z; D, A, B, C, s) = 2 \int_0^{\frac{1}{\sqrt{1+s}}} \frac{\left(\frac{\bar{m}}{R_e}\right)^{-p} e^{-b_n \left(\frac{\bar{m}}{R_e}\right)^{1/n}} \xi^2 d\xi}{\tilde{d}_2(\xi; D, A, B, C)}, \quad (36)$$

where

$$\bar{m}^2 = \xi^2 \left[\frac{x^2}{1 + (a^2 - 1)\xi^2} + \frac{y^2}{1 + (b^2 - 1)\xi^2} + \frac{z^2}{1 + (c^2 - 1)\xi^2} \right], \quad (37)$$

and

$$\tilde{d}_1(\xi; A, B, C) \equiv \sqrt{(1 + (A - 1)\xi^2)(1 + (B - 1)\xi^2)(1 + (C - 1)\xi^2)}, \quad (38)$$

$$\tilde{d}_2(\xi; D, A, B, C) \equiv (1 + (D - 1)\xi^2) \tilde{d}_1(\xi; A, B, C). \quad (39)$$

Total mass of the galaxy represented by our new triaxial model is easily found to be

$$M_{TG} = 2\alpha \left[\frac{r_b^3}{3 - \gamma} + \bar{\rho} R_e^3 n b^{n(p-3)} \Gamma \left[n(3-p), b \left(\frac{r_b}{R_e} \right)^{1/n} \right] \right]. \quad (40)$$

To “normalize” our model to have the total mass equal to unity, the expressions for potential and forces need to be divided by M_{TG} .

In the spherical limit, $a = b = c = 1$, the expressions of Terzić & Graham (2005) are recovered (see Appendix A).

2.3 Special Case $r_b = 0$: Triaxial Generalization of Prugniel–Simien Profile

In the limit of the break radius r_b going to zero, our two-regime model reduces to a single regime Sérsic profile. The corresponding equations for mass density, potential and forces for this triaxial profile are readily obtained after setting $r_b = 0$ in the equations (2), (11) and (26), respectively, and are given by

$$\rho(m) = \rho_b \bar{\rho} \left(\frac{m}{R_e} \right)^{-p} e^{-b_n (m/R_e)^{1/n}}, \quad (41)$$

$$\Phi(x, y, z) = -\alpha n \bar{\rho} R_e^2 b_n^{n(p-2)} T(x, y, z; a^2, b^2, c^2, \infty), \quad (42)$$

$$F_{q_i}(x, y, z) = -\alpha \bar{\rho} q_i S(x, y, z; k_i^2, a^2, b^2, c^2, \infty), \quad (43)$$

Total mass for the Prugniel–Simien model is readily obtained by substituting $r_b = 0$ into (40):

$$M_{PS} = 2\alpha \bar{\rho} R_e^3 n b^{n(p-3)} \Gamma [n(3-p)]. \quad (44)$$

2.4 Special Case $r_b = \infty$: Triaxial Power-Law Core

In the limit of the break radius r_b tending to infinity, our two-regime model reduces to a single power-law core profile. The equations for mass density, potential and forces for the 3D power-law core are given by

$$\rho(m) = \rho_b \left(\frac{r_b}{m} \right)^\gamma, \quad (45)$$

$$\Phi(x, y, z) = \alpha \frac{1}{2 - \gamma} r_b^\gamma r^{2 - \gamma} H(x, y, z; a^2, b^2, c^2, 2 - \gamma), \quad (46)$$

$$F_{q_i}(r, \theta, \phi) = -\alpha r_b^\gamma q_i H_2(x, y, z; k_i^2, a^2, b^2, c^2, -\gamma), \quad (47)$$

For some special cases, such as $\gamma = 0, 1, 2$, the above expressions are given in terms of elementary functions and Carlson integrals (de Zeeuw & Pfenniger 1988; Poon & Merritt 2001). Single power-law model is scale-free, which means that orbital properties simply scale with radius. This property leads to the separation of radial and angular dependence in spherical coordinates, thus allowing for efficient series approximation, such as double Fourier or Fourier-Legendre (Terzić 2002).

Total mass for the power-law core is readily found to be

$$M = \frac{2\alpha}{3 - \gamma} r_{\max}^3, \quad (48)$$

where r_{\max} is the outer radius of the core.

2.5 Non-Dimensionalizing the Physical Problem

In order to make the numerical problem dimensionless, we adopt a convention $G = M_{\text{tot}} = M_{TG} = M_{PS} = M_D = 1$. This means that, since

$$\begin{aligned} G &= 6.672 \times 10^{-11} [\text{kg}]^{-1} [\text{m}]^3 [\text{sec}]^{-2} \\ &= [10^{11} M_\odot]^{-1} [\text{kpc}]^3 [1.491 \times 10^6 \text{yr}]^{-2}, \end{aligned} \quad (49)$$

the unit of time is

$$1.491 \times 10^6 \text{yr} \sqrt{\frac{M_\odot 10^{11}}{M} \left(\frac{\beta}{1 \text{kpc}} \right)^{\frac{3}{2}}}, \quad (50)$$

where β is the length-scale of the model. The total stellar mass can be easily computed from the best-fit parameters of three models, via equations (40), (44) and (C2). If the observed effective half-light radius is taken to be the length-scale of the model β (see Table 2), respective time-scales are easily computed using expression (50). Each unit of length corresponds to 1 kpc.

3 NUMERICAL IMPLEMENTATION

In this Section we outline the major features of the numerical suite which we designed to optimize orbit integrations in the new triaxial potential – triaxial generalization of a 5-parameter Terzić–Graham model, as well as its 3-parameter special case (when central core is not depleted) triaxial Prugniel–Simien model.

Our goal is to design a state-of-the-art, user-friendly numerical package which would allow for easy setup and efficient execution of numerical integrations of orbits in the new model. Our suite of numerical routines is thoroughly tested and fully optimized. It is also parallelized using MPI, with its efficiency scaling roughly linearly with the

number of processors used. We make this numerical suite freely available for downloading from our group’s webpage: http://www.nicadd.niu.edu/research/beams/TS_2007/.

3.1 Outline of the Numerical Suite

The numerical suite utilizes a number of tested and optimized non-proprietary numerical packages written in FORTRAN 77. The numerical algorithm used for integrating orbits is the explicit imbedded (7,8) pair of Dormand and Prince to compute orbital points (Hairer, Norsett & Wanner 1993). Complete and incomplete gamma functions are computed by routines from SLATEC, created by American National Laboratories (available online at <http://www.netlib.org/slatec>). Evaluation of quadratures, both with finite and infinite ranges, is done by QUADPACK routines (Piessens, de Doncker-Kapenga & Überhuber 1983), (also available online at <http://www.netlib.org/quadpack>). The driver program is written in FORTRAN 90.

Flow-chart outlining the numerical suite is shown in Fig. 2.

3.2 Modular Design

We designed the integrator core of the numerical package to be as simple as possible while allowing easy addition of multiple models and analysis routines in a parallelized integrator system. The data flow of the system is outlined in Fig. 2. A parameter settings file is defined by the user, which defines settings for the integrator, the initial conditions generator, the potential and forces models, and the analysis routines. This file is first processed by the initial conditions generator to produce an initial conditions file. The integrator core then uses both the parameter settings file and the initial conditions file to begin integrating the orbits. For each orbit, the initial conditions are read directly from the initial conditions file, and the integrator core obtains the forces from the models using the standard “potential and forces” interface in order to perform the total orbital integration. When the integration is complete, orbital data is passed on to the analysis routines, which are responsible for data processing and producing the output file for the simulation.

Every effort is made to separate the user-editable code from the system-level code. This allows the system to be modified for use with any model and analysis routines without requiring changes to the source files containing the integrator or parallelization code. The user can supply any model to the integrator using the standard “potential and forces” interface. This is done by simply filling in the supplied functions `get_acceleration` and `get_potential` with user-specific code. Supplying analysis routines such as an FFT routine or an energy-conservation measurement is similarly trivial, by simply adding code to perform the operation in the `analyze_orbit` routine. More advanced analyses such as tracking Lyapunov exponents or tangent dynamics are obtained through a similar interface which allows an arbitrary number of extra integration variables to be tracked along with the main orbit without changes to the main integrator source code.

We created a parallel implementation of this integrator using MPI by using a block-decomposition technique

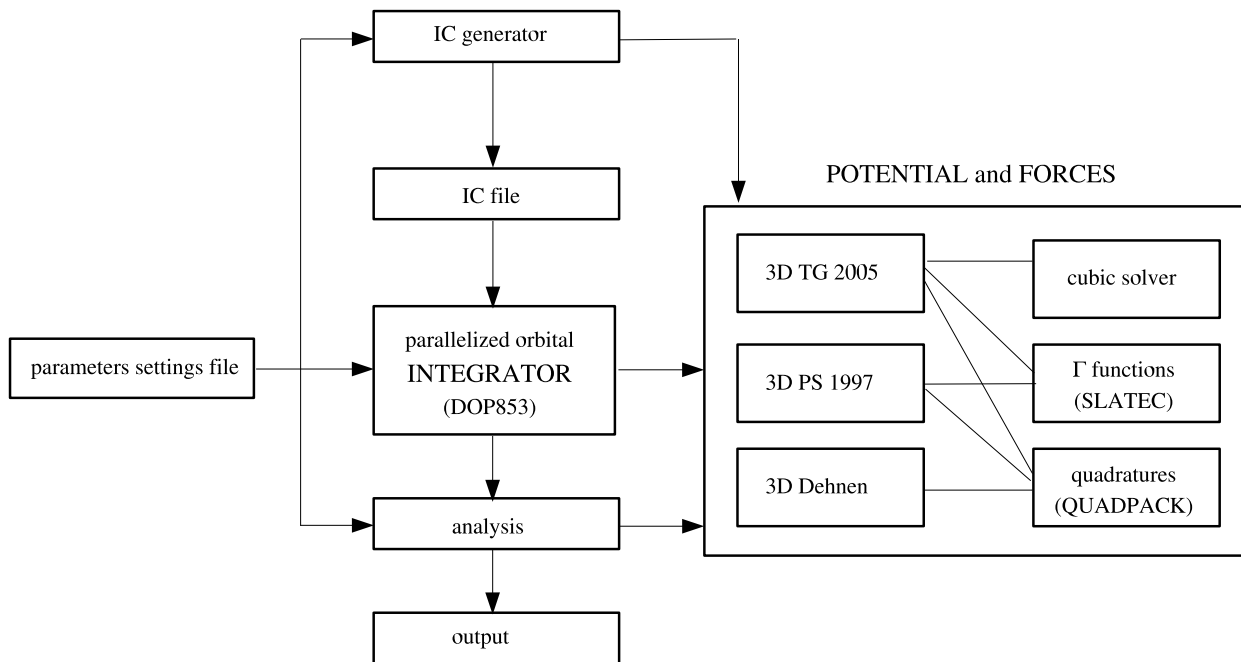


Figure 2. Flow-chart outlining the numerical suite.

to assign nearly equal amounts of orbits to each processor. Each processor computes its orbits one at a time, and writes its output to its own local output file. Once all processors have computed their sets of orbits, the main output file is constructed by concatenating the individual output files together. The final output file contains the orbits in exactly the same order as they were arranged in the initial conditions file because a block-decomposition assignment of orbits is used. The parallel implementation is completely transparent to the user-editable code in the analysis and model definition routines, because the parallel decomposition of the problem is done in groups of orbits in the same manner as the analysis decomposition.

3.3 Parallel Implementation

Our parallel decomposition of the orbital integrator requires very little communication between the computation nodes, which is why we estimate that the speedup derived from parallel computation scales roughly linearly with the number of processors used. However, this nearly optimal speedup is limited by two main factors. First, the number of orbits to integrate must exceed the number of processors. This is required in order to allow each processor to contribute toward the overall solution. Second, the length of time to integrate each orbit must be approximately equal, because the algorithm is not finished until the slowest processor has completed its equal sized block of orbit integrations.

In common use of this integrator, however, these factors are not expected to play a large role in the actual performance of the simulation. The first problem is averted by the fact that integration batches are commonly grouped in larger numbers than are typical for a multiple-processor cluster. Common clusters have processor counts in the hundreds, while it is often desirable to run integration groups num-

bering from hundreds to thousands of stars in each energy level. The second problem is avoided because it is common practice to group initial conditions in batches according to energy level. Since the dynamical time is roughly equal for all stars of the same energy level, we can say that all integrations of the same simulation time length will take approximately the same amount of real time to simulate. One exception to this is the fact that centrophilic orbits, ones with no angular momentum, typically take longer to integrate: the integrator is forced to take increasingly smaller steps near the very center in order to attain prescribed accuracy when orbits' velocities are high. This is why in our numerical suite generates initial conditions for centrophilic orbits (vanishing angular momentum) separately from the centrophobic ones (see Appendix B). Therefore, if these two types of orbits are integrated separately, the roughly linear scaling of simulation time with the number of processors is preserved.

4 MODEL COMPARISON

The Dehnen model and simple power-law core models have been quite popular as *qualitative*, “toy” models which capture general features of stellar dynamics near galactic centers (Merritt & Fridman 1996; Valluri & Merritt 1998; Merritt & Valluri 1999; Poon & Merritt 2001; Terzić 2002). By devising parametric models which provide excellent fits to the full range of the observed data, not only the central region, we are now in position to develop *quantitative* models for individual galaxies.

Here we propose the 3-parameter triaxial generalization of Prugniel-Simien model as an alternative to the 3-parameter Dehnen model for modeling dynamics of elliptical galaxies without depleted cores. For the galaxies with

depleted cores, we propose a triaxial generalization of the 5-parameter Terzić–Graham. We first reiterate the findings of Terzić & Graham (2005) that these alternatives provide much better fits to deprojected observed light-profiles of realistic galaxies using two representative examples from their set of eight elliptical galaxies and the bulge of the Milky Way. We then demonstrate that using these improved triaxial models in dynamical simulations will not incur appreciable additional computational cost over the traditional Dehnen model. It is our belief that having a considerably more accurate model of the observed physical system more than justifies the modest increase in computational expenses.

4.1 Fitting Realistic Deprojected Light-Profiles

Terzić & Graham (2005) fitted several of the most popular density models: 2-parameter Jaffe (1980) and Hernquist (1990); 3-parameter Dehnen and Prugniel–Simien; and their own new 5-parameter hybrid model to deprojected light profiles of several elliptical galaxies. For their sample of luminosity-density profiles taken from real galaxies the 2-parameter Jaffe and Hernquist double power-law models systematically fail to fit the entire extent of observed galaxy profiles. The 3-parameter Dehnen model does better, providing a good match to density profiles of large early-type galaxies with Sérsic index around 4 or greater, but it is inadequate for galaxies with low Sérsic indices, which include dwarf ellipticals and most bulges in disk galaxies. The 3-parameter Prugniel–Simien model, however, accurately matches the density profiles of *both* luminous elliptical galaxies with $n > 4$ and faint elliptical galaxies with $n < 4$, including exponential ($n = 1$) profiles. For galaxies with partially depleted cores, Terzić & Graham (2005) developed a 5-parameter, two-regime model, capable to match simultaneously *both* the nuclear and global stellar distribution. Terzić & Graham (2005) arrive to these conclusions after fitting a set of eight elliptical galaxies of various sizes and light-profile shapes.

In the present study, we focus on the bulge in the center of the Milky Way and the two galaxies from the sample used in Terzić & Graham (2005): an elliptical galaxy NGC 1379, and an elliptical galaxy with partially depleted core – NGC 3348. The Milky Way’s bulge and the first galaxy, NGC 1379, with Sérsic index of $n = 2.0$ (see Table 2 of Terzić & Graham 2005), were chosen because it illustrates that Dehnen is inadequate to describe galaxies with low Sérsic indices, and that Prugniel–Simien model is a good alternative. The second galaxy, NGC 3348, is an example of a galaxy with partially depleted cores for which only 5-parameter Terzić–Graham model provides good fits in density space.

The profiles have been calibrated in units of $L_{\odot} \text{ pc}^{-3}$ using the distance moduli provided in Tonry et al. (2001) for NGC 1379 and the distance of 41 Mpc for NGC 3348. We used solar absolute magnitudes of $M_K = 3.33$, $M_B = 5.47$ and $M_R = 4.28$ (Cox 2000). A Hubble constant $H_0 = 75 \text{ km s}^{-1} \text{ Mpc}^{-1}$ is used.

In the top two rows of Fig. 3, the 3-parameter Dehnen and Prugniel–Simien models were fitted to the deprojected major-axis K -band light-profile of the Milky Way’s bulge (first row) and B -band light-profile of NGC 1379 (second

row). It is clear that Dehnen model is morphologically inadequate to provide a good fit for these types of galaxies which have a low value of Sérsic index n . Prugniel–Simien model does better, especially fitting the outer curvature of the profile, as evidenced by the smaller relative error $\delta(r)$. In the bottom row of Fig. 3, the 3-parameter Dehnen and Prugniel–Simien models, along with the 5-parameter Terzić–Graham were fitted to the deprojected major-axis R -band light-profile of a core elliptical galaxy NGC 3348. Both Dehnen and Prugniel–Simien models fail to account for the inner partially depleted core. The 5-parameter Terzić–Graham model does quite well and is the only density model that can fit galaxies possessing depleted cores.

Fig. 4 shows the total enclosed stellar mass, potential and forces for the models from Fig. 3, using the best-fitting parameters reported in Table 2. The deviations in these quantities outside the range over which the data exists (as denoted by vertical lines) is the result of models being different in extrapolation.

4.2 Computational Efficiency

The quadratures involved in computing forces for the Dehnen model are similar to those used for Prugniel–Simien and Terzić–Graham models (compare the equation (C6) to equations (25)-(26) and (43)). It is therefore reasonable to expect that alternative implementations of the numerical evaluation of these quadratures will be equally reflected on the computational speeds. In other words, the relative computational efficiency outlined later in the Section should be general.

It is possible to considerably improve computational efficiency of force computations by exploiting simplifications arising for special cases of parameters (e.g. integer values of the central cusp γ_D for the Dehnen model) or galaxy shapes (e.g. spherical case $a = b = c = 1$). These simplifications were exploited in the earlier, *qualitative* studies featuring the Dehnen model, in which $\gamma_D = 0$ represented the model with no central cusp, $\gamma_D = 1$ “weak” and $\gamma_D = 2$ “strong” central cusp (Friedman & Merritt 1996, Siopis 1999). However, for *qualitative* studies such as the one we are proposing here, it is not expected for deprojected galaxy profiles to be best fitted by parameter values which take on these fortuitous values, which is why these simplifications arising from special cases are not explored here.

4.3 Comparing Speed of Orbital Integration

We now compare numerical efficiency of orbital integrations of the two new models – Terzić–Graham and its special case Prugniel–Simien – with the traditional Dehnen model for a typical galaxy. (Expressions for density, potential and forces for the Dehnen model are given in Appendix C.) We compare integration times for equivalent sets of orbits in the three models obtained after parametric fitting in density space to the deprojected light-profile of NGC 3348 (Table 2).

In comparing the computational speeds of various models against one another, it is necessary to determine a setting which provides a fair comparison. On the surface, it seems that comparing run times for orbital integrations of equal integration time would be a reliable setting. In fact, this is

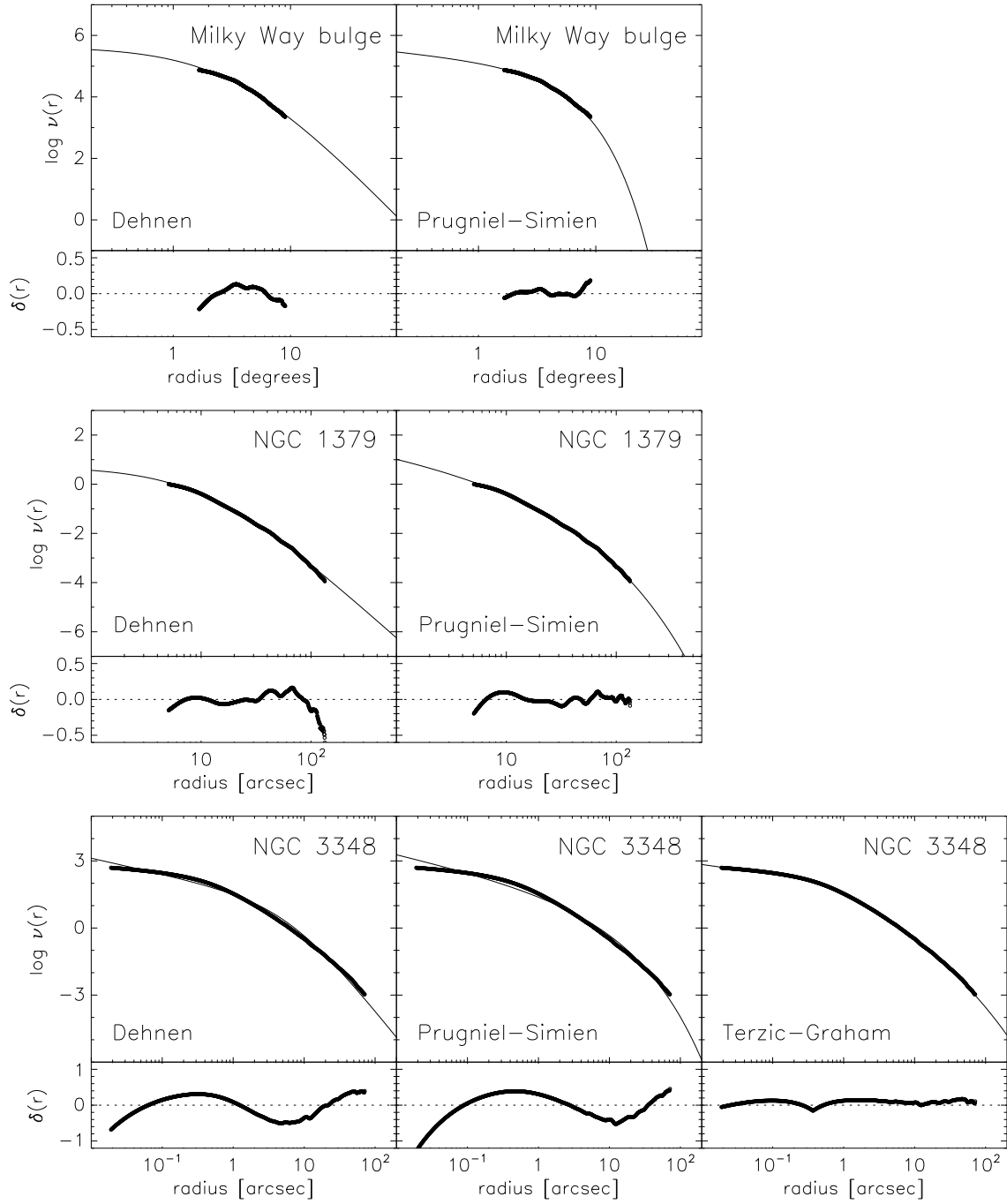


Figure 3. Top row: parametric fits (along with the relative error shown underneath) of Dehnen model (left), Prugniel-Simien model (right) to the deprojected major-axis, K -band light profiles of the central bulge in the Milky Way (fitted out to $R = 9$ degrees; data from Kent, Dame & Fazio 1991). Middle row: parametric fits (along with the relative error shown underneath) of Dehnen model (left), Prugniel-Simien model (right) to the deprojected major-axis, B -band light profiles of NGC 1379 elliptical galaxy (data from Caon, Capaccioli & D’Onofrio 1993). Bottom row: parametric fits (and relative errors) of Dehnen model (left), Prugniel-Simien model (middle) and Terzić-Graham (right) to deprojected major-axis, R -band light profiles of NGC 3348 elliptical galaxy (data from Trujillo et al. 2004). The luminosity-density profile $\nu(r) = \rho(r)/(M/L)$ is in units of $L_{\odot} \text{ pc}^{-3}$. The model parameters are given in Table 2.

Table 1. For the bulge at the center of the Milky Way, NGC 1379 and the core galaxy NGC 3348: total stellar mass, unit of model (simulation) time in physical time and the Hubble time (1.37×10^{10} years) in terms of model (simulation) time, as computed from the parameters for the three models via equation (50). We adopt the observed half-light radius computed from Sérsic and core-Sérsic fits to projected light-profiles, reported in Table 2 of Terzić & Graham (2005), as the length-scale β . Mass-to-light ratios are taken to be $M/L = 0.66$ for the K -band, $M/L = 3$ for the R -band, and $M/L = 5.3$ for the B -band (Worthey 1994).

Gal. Id.	β [arcsec]	Model	Total stellar mass [M_{\odot}]	Unit of time [years]	T_{Hubble} [model units]
Milky Way	1.65×10^4	Dehnen	1.08×10^9	4.43×10^6	3.09×10^3
		Prugniel–Simien	4.87×10^8	6.60×10^6	2.08×10^3
NGC 1379	24.3	Dehnen	5.93×10^{10}	4.50×10^6	3.04×10^3
		Prugniel–Simien	5.02×10^{11}	4.90×10^6	2.78×10^3
NGC 3348	21.4	Dehnen	1.86×10^{11}	6.11×10^6	2.24×10^3
		Prugniel–Simien	1.76×10^{11}	6.29×10^6	2.18×10^3
		Terzić–Graham	1.72×10^{11}	6.37×10^6	2.15×10^3

Table 2. Best-fitting parameters from the three density models over the entire range of the deprojected profile. The units are $L_{\odot} \text{pc}^{-3}$ for ρ and arcseconds for R_e , r_a and r_b .

Gal. Id.	Band	Dehnen			Prugniel–Simien			Terzić–Graham				
		r_a	$\log \rho(r_a)$	γ_D	R_e	$\log \rho(R_e)$	n	R_e	n	γ	r_b	$\log \rho(r_b)$
Milky Way bulge	K	1.258×10^4	-7.339	0.00	1.438×10^4	-7.406	0.884
NGC 1379	B	11.1	-0.49	0.00	24.7	-1.31	2.10
NGC 3348	R	6.40	0.14	0.71	13.227	-0.634	2.124	20.2	3.6	0.44	0.37	2.15

the case when using a constant time-step ordinary differential equation (ODE) solver, because it guarantees that the `get_acceleration` routine will be called an identical number of times for each model.

However, restricting the orbital integrator to constant time-step solvers is not desirable because of their poor performance when compared to adaptive-step solvers. Adaptive-step solvers adjust the size of the integration step so as to satisfy the predefined error tolerance. Simulation time for integrations using adaptive-step ODE solver only obtains physical significance when scaled to *dynamical time* of the orbit at a certain energy level. In this setting, we define the dynamical time to be the average period of an oscillation of a star around the origin of the galaxy.

For the NGC 3348 (parameters are given in Table 2), we integrated 600 box orbits and 600 tube orbits (see Appendix B) at 50 logarithmically spaced energy levels in the range $E(10^{-2}\beta) \leq E(r) \leq E(5\beta)$ (where $E(r) = \Phi(r, 0, 0)$ denotes a isoenergy surface pierced by the x -axis at $x = r$), for roughly 3 Hubble times (length-scale β and Hubble times are given in Table 1). We used a maximally triaxial axis ratio $((a^2 - b^2)/(a^2 - c^2) = 0.5)$ $a : b : c = 1 : 0.79 : 0.5$.

Figure 5 shows the total simulation time. The Prugniel–Simien is consistently about 40 – 80% slower than the Dehnen model, while Terzić–Graham, on average, is at least as fast as the Dehnen model. There is a “bump” in the line corresponding to the Terzić–Graham model around the break radius. This is due to the fact that the adaptive-step ODE integrator samples the region around the transition more densely, which results in increase in the total simulation times.

Increasing the steepness of the negative central density slope (γ_D for Dehnen, γ for Terzić–Graham and p for Prugniel–Simien) of the model renders orbital integration more computationally intensive, because of the rapid changes in the forces. For NGC 3348, the central density slopes of the Dehnen ($\gamma_D = 0.71$) is nearly identical to that of the Prugniel–Simien ($p = 0.72$), but somewhat larger than

that of Terzić–Graham ($\gamma = 0.44$). This means that the comparison of execution speeds for orbits in potentials modeling NGC 3348 will accurately reflect efficiency of force evaluations in the Prugniel–Simien model relative to that of the Dehnen model, while the Terzić–Graham will have a slight “advantage”, having the shallower central slope. This is indeed what we see in Fig. 5: the 5-parameter Terzić–Graham model outperforms both 3-parameter models – the traditional Dehnen and the Prugniel–Simien – mostly because of its shallower central cusp.

The full 5-parameter version of the Terzić–Graham model should only be used to model galaxies with depleted cores, which means that it would *always* have shallower inner slopes than their Dehnen or Prugniel–Simien counterparts, and therefore be computationally very competitive with them, often even outperforming them (the exact performance depending on the level of depletion of the core).

The special case of the 5-parameter Terzić–Graham, the 3-parameter Prugniel–Simien, should only be used to model galaxies without depleted cores. In those cases, the computational price to pay over the traditional Dehnen model is modest – about 40 – 80% over the meaningful range of energies. We believe that having a quantitative model appreciably more faithful to the physical problem is well worth the price.

5 SUMMARY

Motivated by the findings of earlier studies (Graham et al. 2002, 2003; Terzić & Graham 2005) which demonstrate that the traditional power-law density models, such as 3-parameter Dehnen, are inadequate to describe density profiles whose slopes continuously vary as a function of radius – as is the case for most elliptical galaxies and bulges – we introduce a new family of realistic triaxial density–potential–force profiles for stellar systems and dark matter halos. The new family is a 5-parameter, two-regime model

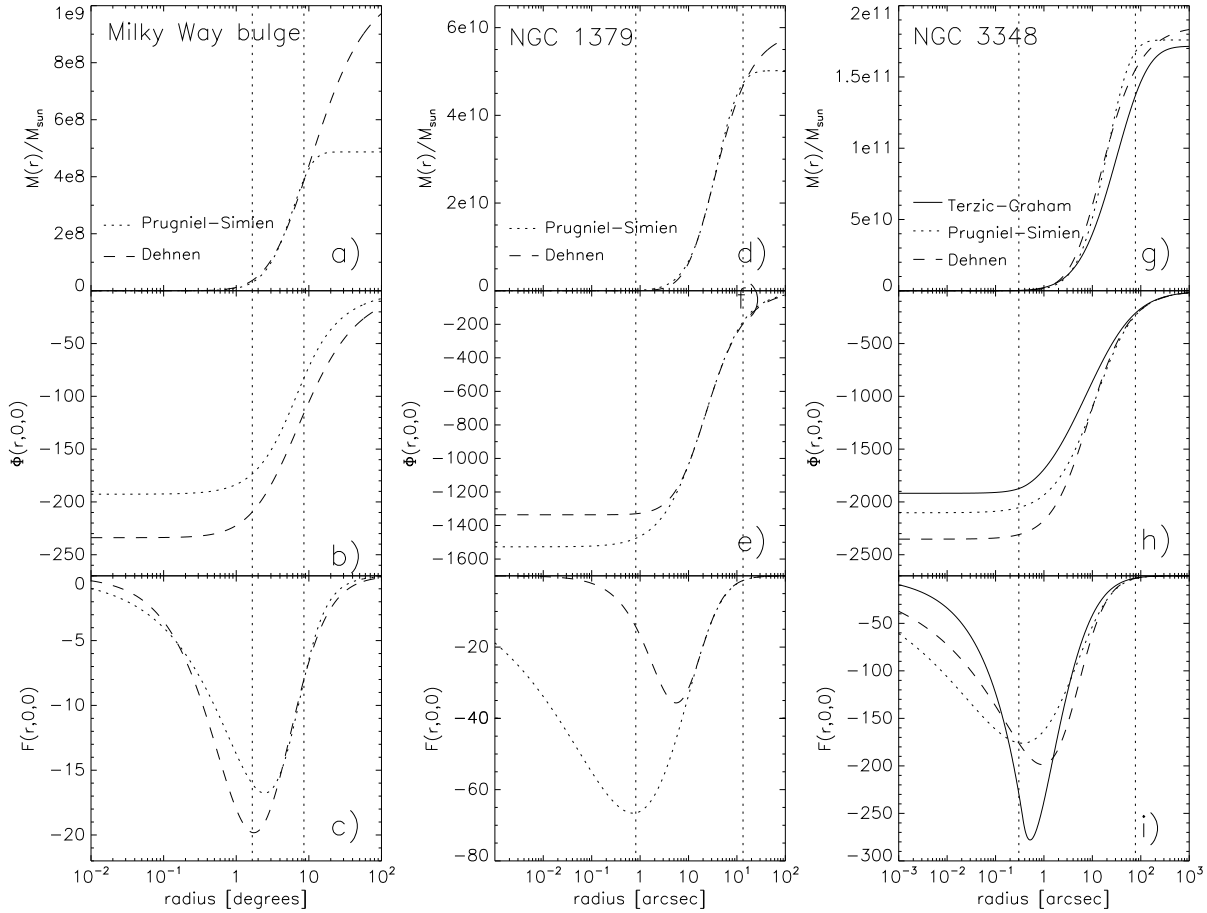


Figure 4. Top column: mass enclosed within radius r in terms of M_{\odot} (top), potential (middle) and force (bottom), along the x -axis, for a spherical Dehnen model (dashed lines) and Prugniel–Simien model (dotted lines) for the Milky Way bulge. Middle column: mass enclosed within radius r in terms of M_{\odot} (top), potential (middle) and force (bottom), along the x -axis, for a spherical Dehnen model (dashed lines) and Prugniel–Simien model (dotted lines) for NGC 1379 elliptical galaxy. Right column: mass enclosed within radius r in terms of M_{\odot} (top), potential (middle) and force (bottom), along the x -axis, for a spherical Dehnen model (dashed lines), Prugniel–Simien model (dotted lines) and Terzić–Graham (solid lines) for NGC 3348 elliptical galaxy. The model parameters are given in Table 2. The axis ratios are 1 : 1 : 1. Vertical dashed lines denote the range over which the data exists. The deviations in mass M , potential Φ , and force F outside this range are the result of models being different in extrapolation.

of inner power-law density core and the outer deprojected Sérsic profile, with the boundary between the two regimes being the break radius r_b . For extreme values of the break radius the model reduces to the 3-parameter deprojected Sérsic $R^{1/n}$ profile ($r_b \rightarrow \infty$) and the 2-parameter power-law core ($r_b \rightarrow 0$). The full 5-parameter model is invoked only when modeling elliptical galaxies with depleted cores; in other cases, which comprise the majority of observed elliptical galaxies and bulges, the 3-parameter triaxial deprojected Sérsic model suffices.

In Section 2, we derived the potential and forces for the fully triaxial density model first presented in its spherical form by Terzić & Graham (2005). Potential and forces are expressed in terms of easy-to-evaluate quadratures. In Section 3, we developed an optimized suite of numerical routines designed for use in orbital integrations.

The goal of this study was to develop and offer to the community an alternative to the traditional Dehnen model which is substantially more faithful to the physical prob-

lem (as measured by the quality of fits to deprojected light profiles) at an almost marginal computational expense.

6 ACKNOWLEDGMENTS

We are happy to thank Alister Graham for his helpful comments and suggestions. We are grateful to Nicola Caon for providing us with the light-profiles for NGC 1379 and to Peter Erwin for kindly supplying us with the light-profile for NGC 3348. B.J.S. is supported by NICADD grant G1A62214.

REFERENCES

- Balcells M., Graham A.W., Dominguez-Palmero L., Peletier R., 2003, *ApJ*, 582, L79
 Caon N., Capaccioli M., D’Onofrio M., 1993, *MNRAS*, 265, 1013
 Carlson B.C., 1988, *Math. Comput.* 51, 267

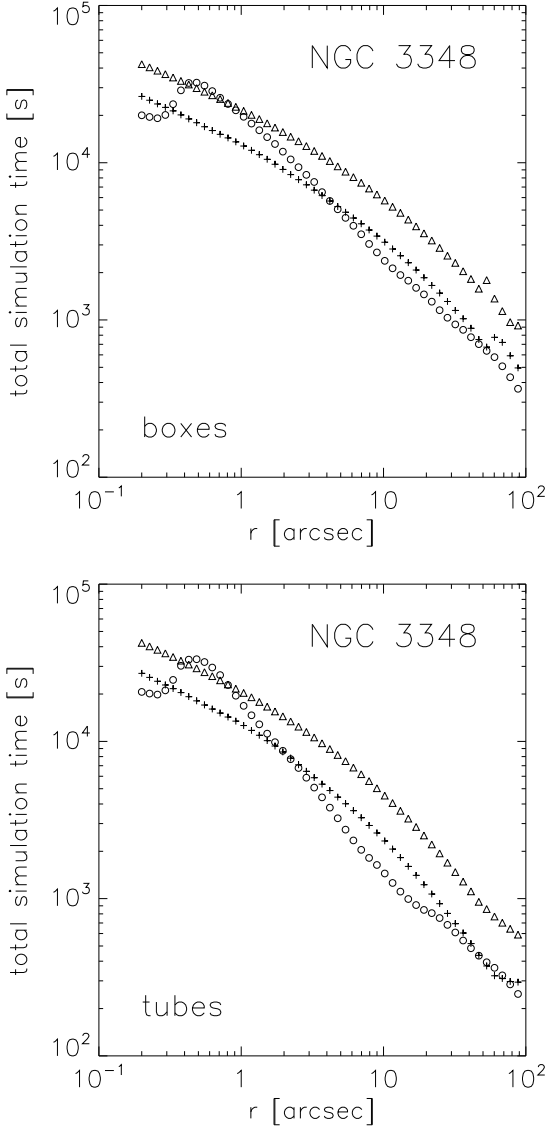


Figure 5. Total simulation time for 600 orbits at varying energy levels (denoted by the maximum radial excursion r) in potentials approximating NGC 3348 galaxy, integrated for the equivalent of 3 Hubble times. Box orbits are shown in the top panel and tube orbits in the bottom. The geometry is maximally triaxial (axis ratio 1 : 0.79 : 0.5). The crosses represent Dehnen model, triangles Prugniel–Simien and circles Terzić–Graham.

Chandrasekhar S., 1969, *Ellipsoidal Figures of Equilibrium*, New York: Dover
 Cox D.P., 2000, *Allen’s Astrophysical quantities*, New York: AIP Press; Springer, p.341
 Dehnen W., 1993, *MNRAS*, 265, 250
 de Vaucouleurs G., 1948, *Annales d’Astrophysique*, 11, 247
 de Vaucouleurs G., 1959, in *Handbuch der Physik*, ed. S. Flügge, Springer, Berlin, p. 275
 de Zeeuw P.T., Pfenniger D., 1988, *MNRAS*, 235, 949
 Fridman T.J., Merritt D., 1996, *AJ*, 114, 1479
 Graham A.W., Erwin P., Trujillo I., Asensio Ramos A., 2002, in Ho L.C. ed., *Carnegie Observatories Astrophysics Series*, Vol. 1: *Coevolution of Black Holes and Galaxies*. Carnegie

Observatories, Pasadena
 Graham A.W., 2001, *AJ*, 121, 820
 Graham A.W., Erwin P., Trujillo I., Asensio Ramos A., 2003, *AJ*, 125, 2951
 Graham A.W., Guzmán R., 2003, *AJ*, 125, 2936
 Graham A.W., Lauer T.R., Colless M.M., Postman M., 1996, *ApJ*, 465, 534
 Graham A.W., Merritt D., Moore B., Diemand J., Terzić B., 2006, *AJ*, 132, 2701
 Hairer E., Norsett S.P. Wanner G., 1993, *Solving Ordinary Differential Equations*, Dover, New York
 Hernquist L., 1990, *ApJ*, 356, 359
 Jaffe W., 1983, *MNRAS*, 202, 995
 Kent S.M., Dame T.M, Fazio G, 1991, *ApJ*, 378, 131
 Kormendy J., Djorgovski S., 1989, *ARA&A*, 27, 235
 Lauer T.R., et al., 1995, *AJ*, 110, 2622
 MacArthur, L.A., Courteau, S., Holtzman, J.A. 2003, *ApJ*, 582, 689
 Merritt D., Fridman T.J. 1996, *ApJ*, 460, 130
 Merritt D., Valluri M. 1999, *AJ*, 118, 1177
 Merritt D., Graham A.W., Moore B., Diemand J., Terzić B., 2006, *AJ*, 132, 2685
 Navarro, J.F., Frenk, C.S., White, S.D.M. 1996, *ApJ*, 462, 563
 Piessens R., de Doncker-Kapenga E., Überhuber C.W., 1983, *QUADPACK: a Subroutine Package for Automatic Integration*, Springer, Berlin
 Prugniel Ph., Simien F., 1997, *A&A*, 321, 111
 Poon M.Y., Merritt D., 2001, *ApJ*, 549, 192
 Schwarzschild M., 1993, *ApJ*, 409, 563
 Sérsic J.L., 1963, *Boletín de la Asociación Argentina de Astronomía*, 6, 41
 Sérsic J.L., 1968, *Atlas de galaxias australes*
 Siopis C., 1999, PhD Thesis, University of Florida
 Terzić B., 2002, PhD Thesis, Florida State University
 Terzić B., Graham A. W. 2005, *MNRAS*, 361, 197
 Tonry J., Blakeslee J.P., Ajhar E.A., Dressler A., 1997, *ApJ*, 475, 399
 Tremaine S., et al., 1994, *AJ*, 107, 634
 Trujillo I., Erwin P., Asensio Ramos A., Graham A.W. 2004, *AJ*, 127, 1917
 Valluri M., Merritt D. 1998, *ApJ*, 506, 686
 Worthey G., 1994, *ApJs*, 95, 107
 Young C.K., Currie M.J., 1994, *MNRAS*, 268, L11
 Zhao H.S., 1996, *MNRAS*, 278, 488

APPENDIX A: SPHERICAL LIMIT

In the spherical limit $a = b = c = 1$, $m = r$ and $\bar{m}(\tau) = \bar{r}(\tau) = r/\sqrt{\tau+1}$ and all quadratures above have analytic solutions given in terms of elementary and special functions:

$$\begin{aligned} H^I(x, y, z; 1, 1, 1, q, s) &= r^q \int_s^\infty (\tau + 1)^{-\frac{3}{2}-q} d\tau \\ &= \frac{2}{1+2q} r^q (s+1)^{-\frac{1}{2}-q}, \end{aligned} \quad (\text{A1})$$

$$\begin{aligned} H(x, y, z; 1, 1, 1, q) &\equiv H^I(x, y, z; 1, 1, 1, q, 0) \\ &= \frac{2}{1+2q} r^q, \end{aligned} \quad (\text{A2})$$

$$R^I(1, 1, 1, s) = \int_s^\infty (\tau + 1)^{\frac{3}{2}} d\tau = \frac{2}{\sqrt{s+1}}, \quad (\text{A3})$$

$$R(1, 1, 1) \equiv R^I(1, 1, 1, 0) = 2, \quad (\text{A4})$$

$$T(x, y, z; 1, 1, 1, s) = \int_0^s \frac{\Gamma \left[n(2-p), b_n \left(\frac{r}{R_e} \right)^{1/n} \right]}{(\tau+1)^{\frac{3}{2}}} d\tau \quad (\text{A5})$$

$$\begin{aligned} &= 2\Gamma \left[n(2-p), b_n \left(\frac{r}{R_e} \right)^{1/n} \right] \\ &\quad - 2\frac{r_b}{r} \Gamma \left[n(2-p), b_n \left(\frac{r_b}{R_e} \right)^{1/n} \right] \\ &\quad + 2\frac{R_e}{r} b_n^{-n} \Gamma \left[n(3-p), b_n \left(\frac{r_b}{R_e} \right)^{1/n} \right] \\ &\quad - 2\frac{R_e}{r} b_n^{-n} \Gamma \left[n(3-p), b_n \left(\frac{r}{R_e} \right)^{1/n} \right], \end{aligned} \quad (\text{A6})$$

$$\begin{aligned} H_l^I(x, y, z; 1, 1, 1, s) &= \log r \int_s^\infty (\tau+1)^{-\frac{3}{2}} d\tau \\ &\quad - \frac{1}{2} \int_s^\infty \frac{\log(\tau+1)}{(\tau+1)^{\frac{3}{2}}} d\tau \\ &= \frac{2}{1+s} \left[\log \frac{r}{\sqrt{1+s}} - 1 \right], \end{aligned} \quad (\text{A7})$$

$$\begin{aligned} H_l(x, y, z; 1, 1, 1) &\equiv H_l^I(x, y, z; 1, 1, 1, 0) \\ &= 2 \log r - 2, \end{aligned} \quad (\text{A8})$$

$$\begin{aligned} H_2^I(x, y, z; 1, 1, 1, q, s) &= r^q \int_s^\infty (\tau+1)^{-\frac{5}{2}-q} d\tau \\ &= \frac{2}{3+2q} r^q (s+1)^{-\frac{3}{2}-q}, \end{aligned} \quad (\text{A9})$$

$$\begin{aligned} H_2(x, y, z; 1, 1, 1, q) &\equiv H_2^I(x, y, z; 1, 1, 1, q, 0) \\ &= \frac{2}{3+2q} r^q, \end{aligned} \quad (\text{A10})$$

$$\begin{aligned} S(x, y, z; 1, 1, 1, s) &= \int_0^s \frac{\left(\frac{r}{R_e} \right)^{-p} e^{-b_n \left(\frac{r}{R_e} \right)^{1/n}}}{(\tau+1)^{\frac{5}{2}}} d\tau \quad (\text{A11}) \\ &= \left(\frac{r}{R_e} \right)^{-p} \int_0^s \frac{e^{-b_n \left(\frac{r}{\sqrt{\tau+1} R_e} \right)^{1/n}}}{(\tau+1)^{\frac{5-p}{2}}} d\tau \\ &= 2nb_n^{n(p-3)} \left(\frac{r}{R_e} \right)^{-3} \Gamma \left[n(3-p), b_n \left(\frac{r}{R_e \sqrt{s+1}} \right)^{1/n} \right] \\ &\quad - 2nb_n^{n(p-3)} \left(\frac{r}{R_e} \right)^{-3} \Gamma \left[n(3-p), b_n \left(\frac{r}{R_e} \right)^{1/n} \right]. \end{aligned} \quad (\text{A12})$$

The result for $T(x, y, z; 1, 1, 1, s)$ is derived after integration by parts. τ_b is easily found from $r_b = r/\sqrt{\tau+1}$.

After some straightforward yet tedious algebra, the equations for mass density, potential and forces reduce to those of Terzić & Graham (2005), their equations (6), (8) and (14), respectively.

APPENDIX B: INITIAL CONDITIONS GENERATOR

Sampling of the initial condition space is done by employing a two-fold two-dimensional start space, following Schwarzschild (1993): the *stationary start space* which contains initial conditions starting from equipotential surfaces with zero velocities; and the *principal-plane start space* which consists of radially stratified initial conditions which pierce one of the three principal planes with the velocity vector normal to the plane. These start spaces are designed to sample different types of orbits arising in triaxial potentials: stationary start space picks up orbits which have zero-velocity turning points, such as boxes and resonant boxlets, while the principal-plane start space selects mostly tube orbits (Schwarzschild 1993; Terzić 2002). The two start spaces are shown in Fig. B1.

The spherical angles of the stationary start space locations are chosen as in Schwarzschild (1993), with the addition that the number of points can be chosen using a parameter `stat_N`, so that the total number of points on this equipotential surface will be 3 stat_N^2 . The zero-velocity radius of this potential in the given direction is then found, resulting in an exact coordinate for the given initial condition.

We calculated zero-velocity radii using a secant-method search to find the root of $\Phi(r, \theta, \phi) - E = 0$, given the direction angles θ and ϕ . This method results in very fast convergence to the solution, even on the unbounded interval $0 < r < \infty$. Proper convergence of this method does assume, however, that the $\Phi(r, \theta, \phi)$ function is monotonically increasing with radius r , which is a condition that is met by the three potential functions considered in this study.

Initial conditions in the principal-plane start space are calculated in a similar manner to Schwarzschild (1993) as well. The parameters `plane_N_theta` and `plane_N_r` determine the number of points sampled. First, the angle θ is subdivided into `plane_N_theta` regions from 0 to $\pi/2$. The centers of each of these regions are chosen as direction vectors within the plane for choosing initial conditions. Along each direction vector, the zero-velocity radius `rmax` is computed as described above. Next, an inner cutoff radius is determined by using a fraction `plane_frac_rmin` such that `rmin = plane_frac_rmin * rmax`. This inner cutoff fraction is a parameter that can be chosen from 0 to 1 in order to reduce the number of orbits that are duplicated at small radii. The initial conditions are then chosen by subdividing the region `rmin` to `rmax` into `plane_N_r` sections, and selecting the center of each section as the location of the initial condition. The velocity is then chosen normal to the plane such that the total energy is equal to the desired energy level. This is done for each of the 3 principal planes, resulting in $3 \times \text{plane_N_theta} \times \text{plane_N_r}$ initial conditions generated in this start space.

APPENDIX C: DEHNEN MODEL

Dehnen model (Dehnen 1993; Tremaine et al. 1994) is a double-power-law, 3-parameter density model, defined by its steepness of the inner cusp γ_D , break radius r_a which marks the transition between the two power-law regimes, and the density at the break radius $\rho(r_a)$:

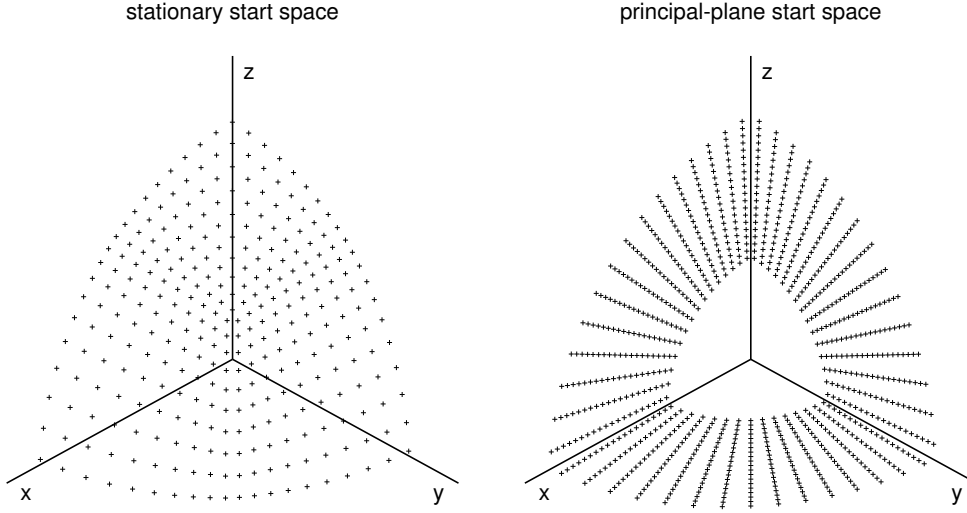


Figure B1. Stationary and principal-plane start spaces.

$$\rho(m) = 2^{4-\gamma_D} \rho(r_a) \left(\frac{m}{r_a}\right)^{-\gamma_D} (r_a + m)^{\gamma_D-4}. \quad (\text{C1})$$

The total mass is easily found to be

$$M_D = \frac{4\pi abc}{3-\gamma_D} r_a^3 2^{4-\gamma_D} \rho(r_a). \quad (\text{C2})$$

The corresponding potential is given by

$$\Phi(x, y, z) = -\frac{GM_D}{2(2-\gamma_D)r_a} \int_0^\infty \frac{P(\bar{m})}{d_1(\tau; a^2, b^2, c^2)} d\tau, \quad (\text{C3})$$

where

$$\begin{aligned} P(\bar{m}) \equiv 1 & - (3-\gamma_D) \left(\frac{\bar{m}}{r_a + \bar{m}}\right)^{2-\gamma_D} \\ & + (2-\gamma_D) \left(\frac{\bar{m}}{r_a + \bar{m}}\right)^{3-\gamma_D} \end{aligned} \quad (\text{C4})$$

This equation is, again, transformed into a proper integral via transformation $\xi = (\tau + 1)^{-1/2}$, to obtain

$$\Phi(x, y, z) = -\frac{GM_D}{(2-\gamma_D)r_a} \int_0^1 \frac{P(\bar{m})}{\tilde{d}_1(\xi; a^2, b^2, c^2)} d\xi. \quad (\text{C5})$$

Similarly, the forces are found to be, after the change of variables,

$$\begin{aligned} F_{q_i}(x, y, z) & = -GM_D(3-\gamma_D)r_a q_i \\ & \times \int_0^1 \frac{\bar{m}^{-\gamma_D} (r_a + \bar{m})^{\gamma_D-4} \xi^2}{\tilde{d}_2(\xi; k_i^2; a^2, b^2, c^2)} d\xi, \end{aligned} \quad (\text{C6})$$

where $k_1 = a$, $k_2 = b$, $k_3 = c$ and $q_1 = x$, $q_2 = y$, $q_3 = z$.